

Research Article

Modeling and analysis of hysteresis using the Maxwell-slip model for variable stiffness actuators

Huibin Qin^{a,*}, Zefeng Zhang^a, Zhili Hou^b, Lina Li^b, Kai Liu^a, Shaoping Bai^c^a School of Mechanical Engineering, North University of China, Taiyuan 030051, China^b College of Mechanical and Vehicle Engineering, Taiyuan University of Technology, Taiyuan 030024, China^c Department of Materials and Production, Aalborg University, Aalborg 9220, Denmark

ARTICLE INFO

Article history:

Received 26 April 2024

Revised 7 June 2024

Accepted 28 June 2024

Available online 3 July 2024

Keywords:

Nonlinear compliant actuators

Elastomer

Maxwell-slip model

Hysteresis modeling

ABSTRACT

Hysteresis non-linearity in variable stiffness actuators (VSAs) causes significant torque errors and reduces the stability of the actuators, leading to poor human–computer interaction performance. At present, fewer hysteresis compensation models have been developed for compliant drives, so it is necessary to establish a suitable hysteresis model for compliant actuators. In this work, a new model with a combination of the Maxwell-slip model and virtual deformation is proposed and applied to an elbow compliant actuator. The method divides the periodic variation of the actuator into three parts: an ascending phase, a descending phase, and a transition phase. Based on the concept of virtual deformation, the nonlinear hysteresis curve is transformed into a polyline, and the output torque is estimated using the revised Maxwell-slip model. The simulation results are compared with the experimental data. Its torque error is controlled within 0.2Nm, which validates the model. An inverse model is finally established to calculate the deformation deflection angle for hysteresis compensation. The results show that the inverse model has high accuracy, and the deformation deflection is less than 0.15 rad.

© 2024 The Author(s). Published by Elsevier B.V. on behalf of Shandong University. This is an open access article under the CC BY-NC-ND license (<http://creativecommons.org/licenses/by-nc-nd/4.0/>).

1. Introduction

The compliance of the exoskeleton flexible elbow joint is reflected in possessing a variable stiffness flexible actuator in terms of mechanical structure, which can enhance the security of application, dynamic adaptability, and flexibility of movement of the robot in the process of interacting with human beings [1,2].

The hysteresis phenomenon in the compliant actuator is manifested as a lag between the application and removal of a force and its subsequent effect, i.e., an obvious nonlinear phenomenon [3]. The existence of the hysteresis nonlinear phenomenon makes it impossible to accurately judge the desirable state of the compliant system, resulting in deviation of the system output, degradation of the motion tracking performance of the actuator, and even system oscillation. Therefore, in order to solve the hysteresis nonlinear problem of compliant actuators, it is significant to propose a model that can describe the hysteresis phenomenon in a real system. At the same time, this model should possess high accuracy and low computational cost.

In recent years, a variety of mathematical models have been developed and applied to piezoelectric ceramics as well as smart material actuators, but few hysteresis models have been used

for compliant actuators [4–6]. Currently, the common hysteresis models are the Preisach model, Bouc-Wen model, Preisach model, Prandtl–Ishlinskii (PI) model, Maxwell-slip model, etc. The Bouc-Wen model describes the hysteresis phenomenon in terms of a non-linear differential equation, which makes the calculation simpler [7]. Nie et al. developed a cascaded Bouc-Wen hysteresis model with linear dynamics, whose identification method fully parallelized the linear and nonlinear parts of the identification task, allowing the identification task to be transformed to linear without iteration. The important reason for the lag phenomenon is the inability to measure and control the internal nonlinear variables. Antonino et al. optimized and identified the unknown parameters of the Bouc-Wen model through the topological optimization method [8]. Wang [9] et al. implemented an asymmetric hysteresis model construction based on the non-hysteresis components of polynomials and identified the hysteresis parameters of the Bouc-Wen model according to an improved differential evolutionary algorithm. However, the differential-based model parameters are limited, and inverse model construction is difficult. Dhaouadi [10] et al. proposed a dynamic system based on the genetic concept for describing hysteresis phenomena in harmonic drives and developed an effective controller. The integral-differential equation to describe the torque-displacement relationship accurately describes complex nonlinear friction. Choi [11] et al. proposed a classical gap

* Corresponding author.

E-mail address: qhbss@163.com (H. Qin).

model based on polynomials and modifications to fulfill three requirements for Series Elastic Actuator (SEA) in rehabilitation robots. That is, the model should first accurately reflect the simulated spring hysteresis characteristics. Secondly, it should reflect the hysteresis differences between different springs. Thirdly, the computational cost of the model should be as low as possible. The two higher-order polynomials used in the model are able to represent the nonlinear with fewer parameters but have the disadvantage of being able to express only up to a third-degree polynomial.

The Preisach model originated from the hysteresis phenomenon in the field of magnetism. Through further development, Everett et al. found that the Preisach model is not limited to the study of material hysteresis in the field of magnetism but that the model is able to be used as a mathematical tool to describe various physical properties of hysteresis [12]. The two sufficient conditions for the Preisach model to represent non-linearity are eras-ability and consistency. However, the hysteresis non-linearity in the real situation does not necessarily satisfy the above two conditions because the Preisach model can only approximate the representation, and then the modeling error will be increased. In operator-based hysteresis models, increasing the number of operators describes the hysteresis model and improves its accuracy, but a large number of coefficients leads to an increase in computational cost. In addition, there is the PI model, the Maxwell-slip model, etc. The PI model belongs to a subset of the Preisach model and is mainly used to model hysteresis in smart materials. The PI model is mainly modeled using two operators: the stop operator and the start operator. However, its inverse model is difficult to construct, and the handling of singularities is particularly difficult to analyze [13]. The Maxwell-slip model was proposed mainly to describe some friction behaviors present in mechanical systems. Zschack [14] proposed an adaptive method based on the generalized Maxwell-slip model for accurate friction compensation. Maxwell-slip modeling identifies force signals applied through unit displacements. Therefore, the method does not require a priori knowledge of physical parameters. Its simplicity in modeling makes it suitable for simulating, hypothesizing, and evaluating system hysteresis phenomena. Rizos [6] proposed a nonlinear regression model based on the Maxwell-slip model and discussed a friction control scheme based on it. Chen [15] and others constructed a new hysteresis model based on the Maxwell-slip model, which incorporates the concept of virtual deformation. The method is computationally simple and easy to construct the inverse model, but the accuracy still needs to be improved. In addition, it is necessary to implement closed-loop feedback and real-time control when the proposed hysteresis model is applied in real-world environments.

From the above analysis, the differential-based model parameters are limited, and inverse model construction is difficult. In operator-based models, the Maxwell-slip model is a suitable choice for compliant actuators. This model has a smaller number of parameters and is therefore relatively straightforward to calculate. Furthermore, no prior knowledge of physical parameters is required. The construction of inverse models is straightforward.

A Maxwell-slip model-based hysteresis modeling methodology is proposed for the investigation of the hysteresis phenomenon observed in the elbow joint actuator. To analyze the hysteresis phenomenon of the actuator, the method of combining virtual deformation is introduced. The torque curve is divided into three parts, namely, an ascending phase, a descending phase, and a transition phase. Comparing the outputs of different models verifies that the proposed hysteresis model has high accuracy. The inverse model of the proposed hysteresis model is developed and analyzed to calculate the variation of the deflection angle to compensate for the elimination of the hysteresis effect.

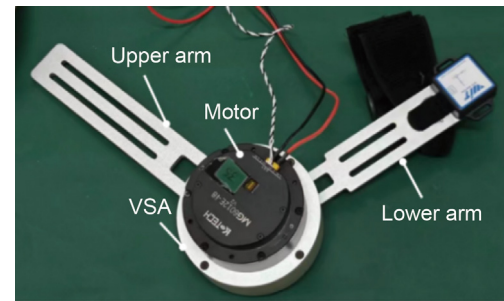


Fig. 1. Elbow joint.

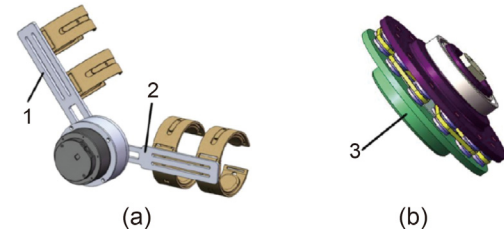


Fig. 2. Compliant Elbow. (a) The overall structure of the variable stiffness compliant elbow joint. (b) The internal variable stiffness driver module.

2. Maxwell-slip modeling of hysteresis in compliant actuators

2.1. Nonlinear compliant actuator for elbow joints

Fig. 1 illustrates a variable stiffness elbow joint device incorporating the non-linear behavior of a compliant actuator. The design was inspired by the concept of a variable stiffness joint proposed by Li and Bai [16,17]. The new device contains an upper arm, a lower arm, a motor, and a VSA [18,19].

The complete structure of the variable stiffness flexible drive elbow joint comprises the big arm, forearm, flexible drive mechanism, and drive device. The overall structure is illustrated in Fig. 1. The large arm 1 is coupled to the small arm 2 and connected to the flexible drive module 3. The rotation axis of the large arm 1 and the small arm 2 is identical, aligning with the movement characteristics of the elbow joint. The relative coupling rotation between the two components can be generated to simulate the flexion and extension of the elbow joint. The overall structure of the variable stiffness compliant elbow joint is shown in Fig. 2(a), and the internal variable stiffness driver module is shown in Fig. 2(b).

Fig. 3 presents the front and back sides of a VSA with 6 compliant branches, where each branch contains 2 pulleys. The elastomer wraps around the pulley and forms a closed loop with the pulley. Varying the number of compliant branches results in different configurations of N , allowing for variable stiffness regulation. The advantages of polyurethane PU are excellent resistance to tension, easy fusion, and easy installation. Therefore, the elastic element is a round polyurethane PU belt, and the diameter of the belt is set to 3 mm. A portion of the input mechanical energy is lost when the elastomer is stretched and compressed. The elastomer deforms, and the output lags behind the input, thus exhibiting hysteresis.

Two methods are currently employed by VSA to adjust variable stiffness. The first method is to alter the configuration of the elastic element in conjunction with the pulley. The second method entails radially adjusting the preload. The transmission principle of the three-jaw chuck is employed to alter the initial length of the elastic element within the compliant actuator,

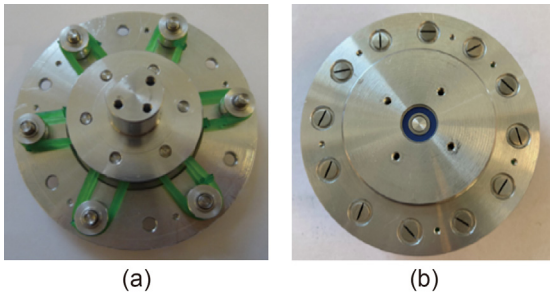


Fig. 3. Physical prototype of VSA. (a) Front side. (b) Back side.

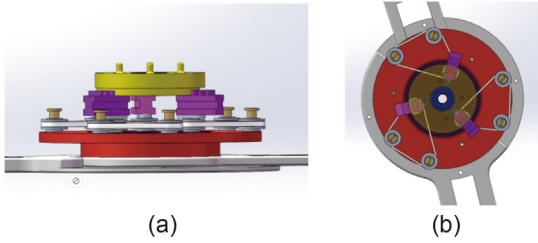


Fig. 4. Radial adjustment of compliant actuator. (a) Main view, (b) Top view.

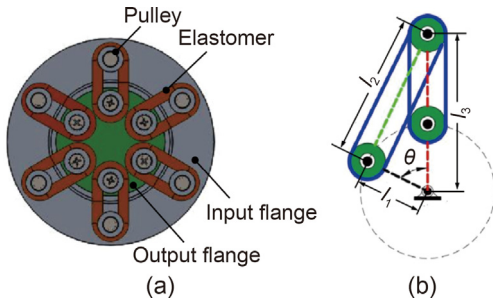


Fig. 5. Variable stiffness compliant actuator with double pulley configuration. (a) Physical prototype with 6 compliant branches ($N = 6$). (b) Mathematical modeling of a single compliant branch.

thereby enabling the radial adjustment of the preload, as shown in Fig. 4.

Fig. 5(a) shows the physical prototype of the VSA. Fig. 5(b) presents the mathematical model of a single compliant branch. The model can be regarded as a special kind of planar four-bar mechanism with frame length 0 , where the elastomer length is l_2 , the crank length is l_1 , and the following link length is l_3 . The elongation length of the elastomer $\delta l_e = 0$ when the deflection angle θ is zero. At this time, $l_1 + l_2 = l_3$. The elongation length of elastomer $\delta l_e = 2(l_1 + l_2 - l_3)$ when deflection angle θ is not zero.

From the figure above, the output torque T is a nonlinear function of the deflection angle θ as the input angle is rotated at θ . Therefore, according to the torque equation and Hooke's law, the torque of VSA can be obtained as

$$T = k [12 (l_1 + l_2 - l_3) + x_0] \frac{l_1 l_3 \sin \theta}{l_2} \quad (1)$$

where k is the stiffness of the elastomer and F_0 is the initial preload of the elastomer. Specific stiffness solutions as well as torque equations are shown in the Appendix.

The polyurethane (PU) round belts used had a strain range of 1.5%–3% and a maximum stretch of 0.7 kg.

For different configurations of N , the curve variation between torque and deflection angle of the actuator is shown in Fig. 6

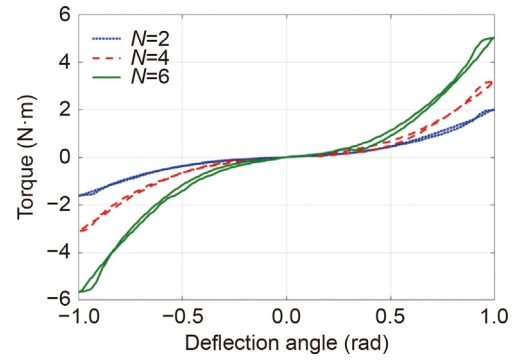


Fig. 6. The variation curve between torque and deflection angle of the VSA in different configurations.

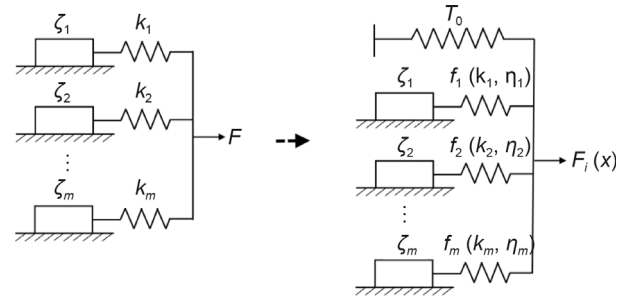


Fig. 7. Correction of Maxwell-slip model.

when the preload force is 5N. The blue curve is the result for $N = 2$ obtained from experimental measurements. The red curve is the result for $N = 4$. The green curve is the result for $N = 6$. All three curves reflect the same hysteresis phenomenon. That is, an ascending curve is shown during the loading phase, and the curve deforms to show another curve during the unloading phase, which has a significant hysteresis effect.

2.2. Maxwell-slip model principle

The Maxwell-slip model operates with an elastic sliding unit composed of a massless linear spring and a massless block that are susceptible to Coulomb friction. The modified Maxwell-slip model is shown in Fig. 7 and contains m elastic units. T_0 is the torque at the turning point of running towards the transition phase [15].

The Maxwell-slip model consists of m parallel elastic units, and each elastic unit is at the same input displacement x . For each unit i , there is a corresponding output force f_i , stiffness k_i , etc., as shown in Fig. 8. The hysteresis force, F_i , is the sum of the initial torque T_0 at the turning point and the sum of the unit forces f_i , as shown in the following equation:

$$F_i(x) = \sum_{i=1}^m f_i + T_0, x \in [x_1, x_2] \cup [x_3, x_4] \quad (2)$$

As seen in Fig. 8, when $k_i > 0$, the instantaneous stiffness of the system S_j is the sum of all k_i . At this time, $S_j > S_{j+1}$, and the hysteresis return line is convex, but the actual torque curve is shown in Fig. 6, and the hysteresis return line is concave, with both positive and negative stiffnesses, which increases the difficulty of obtaining the parameters of the Maxwell-slip model. Therefore, hysteresis modeling considers combining virtual deformation to transform the nonlinearity of the hysteresis phenomenon into a polyline [20].

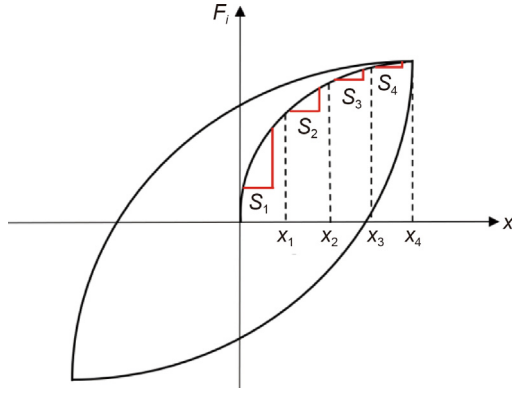


Fig. 8. Sliding behavior of the elastic unit. $S_j = \sum_{i=j}^m k_j$.

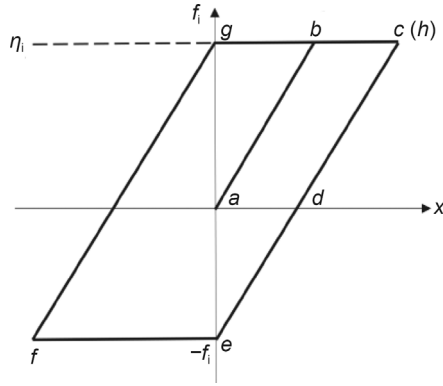


Fig. 9. The hysteresis characteristics of position and force in the Maxwell-slip model.

The modified Maxwell-slip model contains m hysteresis elastic units and torque variables at the transition between the ascending and descending phases. The relationship between the force applied by each elastic unit and the displacement output and its hysteresis behavior is shown in Fig. 9.

From a to b, the spring is gradually elongated, but no movement of the block occurs. The force continues to be applied until it reaches the ultimate slip force η_i and the block starts to slide, continuing to point c, after which the block begins to move in the opposite direction and the spring is compressed until point e. Again, the sliding is started from point e to point f when the applied force reaches force $-f_i$.

The relationship between force and displacement in the Maxwell-slip model is shown as follows:

$$f_i = \begin{cases} k_i(x - \zeta_i), & |k_i(x - \zeta_i)| < \eta_i \\ \eta_i \text{sgn}(\dot{x}), & \zeta_i = x - \frac{\eta_i}{k_i} \text{sgn}(\dot{x}) \end{cases} \quad (3)$$

The k_i is the stiffness of the spring, ζ_i is the initial state position, and η_i is the ultimate slip force.

Based on the principle of virtual work, the relationship between K and θ can be described as $\delta T = K \cdot \delta \theta$. The output torque of the compliant actuator is re-mathematically calculated as shown in Eq. (4)

$$T = Kh(\theta) \quad (4)$$

where T is the output torque, K is the stiffness of the elastomer, and θ is the deviation from the equilibrium position.

Define the virtual deformation x as

$$x = h(\theta) \quad (5)$$

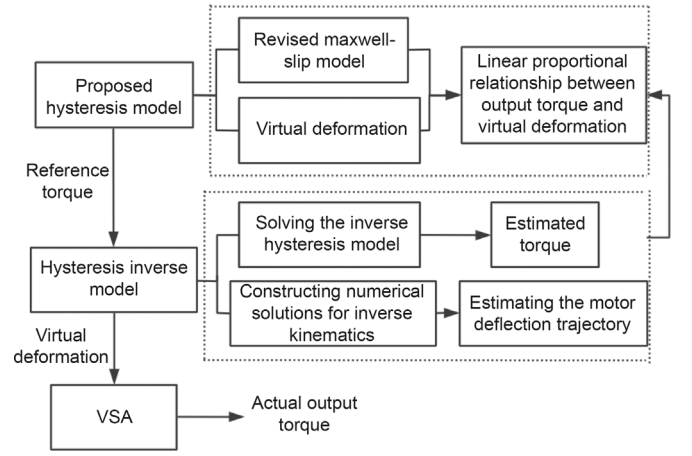


Fig. 10. Block diagram of hysteresis modeling.

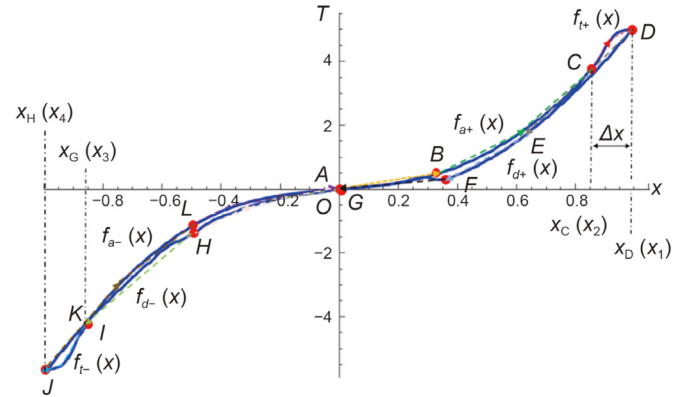


Fig. 11. Constructed hysteresis model.

In configuration $N = 6$, $h(\theta)$ is

$$h(\theta) = [12(l_1 + l_2 - l_3) + x_0] \frac{l_1 l_3 \sin \theta}{l_2} \quad (6)$$

3. Hysteresis modeling for the proposed hysteresis model

The modeling requires the introduction of virtual deformations and combining them with a modified Maxwell-slip model to construct the torque curve, which is easy to construct with high accuracy and low computational effort. The hysteresis behavior can be accurately described using functional relationships. Hence, the inverse model is developed, and the inverse function is solved. In order to design the compensator to eliminate the hysteresis effect, the variation of parameters such as output torque and deflection angle is estimated and calculated. The hysteresis modeling framework is shown in Fig. 10.

The proportional linear relationship between output torque and deflection can be seen from the above equation. The hysteresis model shown in Fig. 11 below is proposed.

The rotation trajectory of the drive period is shown in Fig. 9 as A-B-C-D-E-F-G-H-I-J-K-L-A. The JC is the ascending phase f_a , the CD and the IJ are the transitional phases f_{t+} , f_{t-} , and the DI is the descending phase f_d .

The output torque can be expressed as follows:

$$T = \begin{cases} f_a(x), \dot{x} \geq 0, x < x_2 \\ f_d(x), \dot{x} \leq 0, x > x_1 \\ f_t(x), x_2 < x < x_1 \end{cases} \quad (7)$$

The torque functions of the ascending and descending curves can be described in detail as:

$$f_a(x) = \begin{cases} k_{JK}(x - x_J) + T_J, x \in [x_J, x_K] \\ k_{KL}(x - x_K) + T_K, x \in [x_K, x_L] \\ k_{LA}(x - x_L) + T_L, x \in [x_L, x_A] \\ k_{AB}(x - x_A) + T_A, x \in [x_A, x_B] \\ k_{BC}(x - x_B) + T_B, x \in [x_B, x_C] \end{cases} \quad (8)$$

$$f_d(x) = \begin{cases} k_{HI}(x - x_I) + T_I, x \in [x_I, x_H] \\ k_{GH}(x - x_H) + T_H, x \in [x_H, x_G] \\ k_{FG}(x - x_G) + T_G, x \in [x_G, x_F] \\ k_{EF}(x - x_F) + T_F, x \in [x_F, x_E] \\ k_{DE}(x - x_E) + T_E, x \in [x_E, x_D] \end{cases} \quad (9)$$

where $k_{ij} = \frac{T_i - T_j}{x_i - x_j}$ ($i, j = A, B, C, D, E, F, G, H, I, J, K, L$). The transition line is described by the modified Maxwell-slip model, and the torque function of the transition line can be described as

$$\begin{cases} f_{t+}(x) = \sum_{i=1}^n f_i + T_0, x \in [x_1, x_2] \\ f_{t-}(x) = \sum_{i=1}^n f_i + T_0, x \in [x_3, x_4] \end{cases} \quad (10)$$

$x_1, x_2, x_3,$ and x_4 are the turning points in the ascending and descending lines, respectively, when the transition line passes through turning points.

$$\begin{cases} f_d(x_1) = k(x_1 - x_2) + f_a(x_2) \\ f_a(x_4) = k(x_4 - x_3) + f_d(x_3) \end{cases} \quad (11)$$

where k is the slope of the transition line, which can be expressed as

$$k = \begin{cases} k_+ = \frac{T_D - T_C}{x_D - x_C}, x \geq 0 \\ k_- = \frac{T_I - T_J}{x_I - x_J}, x < 0 \end{cases} \quad (12)$$

Therefore, substituting the above Eqs. (8) and (9) into (11) we can conclude that

$$\begin{cases} x_1 = \frac{f_a(x_2) - kx_2 + p(x_1)}{k(x_1) - k} \\ x_2 = \frac{f_d(x_1) - kx_1 + p(x_2)}{k(x_2) - k} \end{cases} \quad (13)$$

$$\begin{cases} x_3 = \frac{f_a(x_4) - kx_4 + p(x_2)}{k(x_2) - k} \\ x_4 = \frac{f_d(x_3) - kx_3 + p(x_1)}{k(x_1) - k} \end{cases} \quad (14)$$

where

$$p(x_1) = \begin{cases} -x_I k_{HI} + T_I, x_1 \in [x_I, x_H] \\ -x_H k_{GH} + T_H, x_1 \in [x_H, x_G] \\ -x_G k_{FG} + T_G, x_1 \in [x_G, x_F] \\ -x_F k_{EF} + T_F, x_1 \in [x_F, x_E] \\ -x_E k_{DE} + T_E, x_1 \in [x_E, x_D] \end{cases}$$

$$p(x_2) = \begin{cases} -x_J k_{JK} + T_J, x_2 \in [x_J, x_K] \\ -x_K k_{KL} + T_K, x_2 \in [x_K, x_L] \\ -x_L k_{LA} + T_L, x_2 \in [x_L, x_A] \\ -x_A k_{AB} + T_A, x_2 \in [x_A, x_B] \\ -x_B k_{BC} + T_B, x_2 \in [x_B, x_C] \end{cases}$$

$$k(x_1) = \begin{cases} k_{HI}, x_1 \in [x_I, x_H] \\ k_{GH}, x_1 \in [x_H, x_G] \\ k_{FG}, x_1 \in [x_G, x_F] \\ k_{EF}, x_1 \in [x_F, x_E] \\ k_{DE}, x_1 \in [x_E, x_D] \end{cases}$$

$$k(x_2) = \begin{cases} k_{JK}, x_2 \in [x_J, x_K] \\ k_{KL}, x_2 \in [x_K, x_L] \\ k_{LA}, x_2 \in [x_L, x_A] \\ k_{AB}, x_2 \in [x_A, x_B] \\ k_{BC}, x_2 \in [x_B, x_C] \end{cases}$$

x_2 is the turning point between the ascending line and the transition line, and x_1 is the turning point between the descending line and the transition line. In addition, x_4 is the turning point between the ascending line and the transition line, and x_3 is the turning point between the descending line and the transition line. The transition phase starts at x_2 . During the transition phase, the torque changes significantly and the curve undulates. When the transformation reaches x_1 , the transition phase is finished. The deformation value x is updated when the following conditions are met.

$$x \geq x_1, \text{ if } \begin{cases} x - x_p \geq 0 \\ x - x_f \geq 0 \end{cases} \quad (15)$$

$$x \leq x_4, \text{ if } \begin{cases} x - x_p \leq 0 \\ x - x_f \leq 0 \end{cases}$$

In the VSA, the initial position is determined. When the actuator starts to move, the parameters $x_i, T_i,$ and e during the rotational motion in the $A - B - C$ trajectory are still the initial values. The deformation value changes significantly when the actuator continues to rotate to C. The ascending curve gradually slows down and starts to transition to the descending curve. The local deformation value reaches its maximum when it arrives at point D. The virtual deformation value is followed up, and the output torque is calculated using the algorithm during this process. The behavioral description of the transition phase is specifically shown in Fig. 12.

The parametric representation with the modified Maxwell-slip model is able to be obtained when the actuator is rotating regularly, as

$$\begin{aligned} k_1 &= K_{p_1 p_2} - K_{p_2 p_3} \\ k_2 &= K_{p_2 p_3} - K_{p_3 p_4} \\ &\dots \\ k_N &= K_{p_N p_{N+1}} \end{aligned} \quad (16)$$

$$\begin{aligned} \eta_1 &= k_1 \frac{x(P_2) - x(P_1)}{x(P_{N+1}) - x(P_1)} e \\ \eta_2 &= k_2 \frac{x(P_3) - x(P_2)}{x(P_{N+1}) - x(P_1)} e \end{aligned}$$

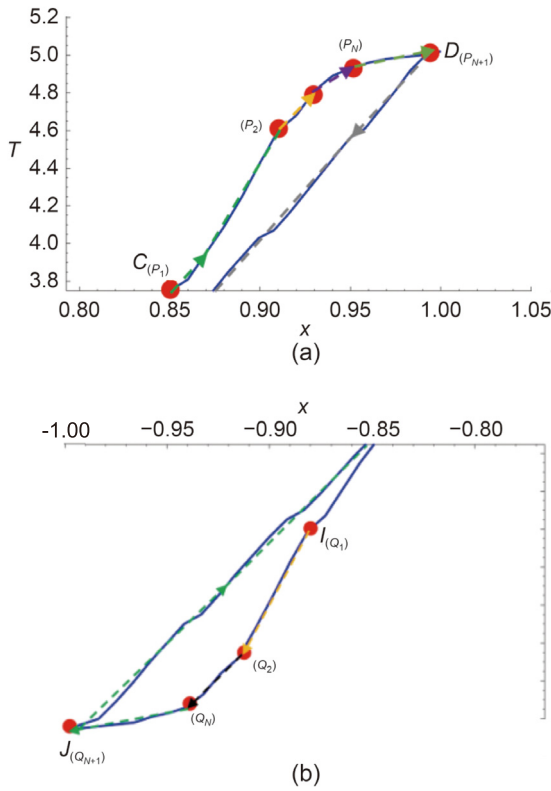


Fig. 12. A detailed behavioral description of the transition phase. (a) Transition phase 1, (b) Transition phase 2.

$$\dots$$

$$\eta_N = k_N e_0 \quad (17)$$

where K , x , and e are the slope of the corresponding crease line, the imaginary deformation value, and the imaginary deformation error in the transition stage, respectively. In some cases, when the system is in the elastic range, the slope difference between two points can be used to approximate the stiffness of the system. Accordingly, the stress and strain of a system in the elastic range are linearly related. The slope can be interpreted as the degree to which the system responds to an external force. Therefore, the difference in slope can be used to indicate the stiffness of the system.

4. Torque test of the proposed hysteresis model

4.1. Measurement and simulation test of the hysteresis model

Torque experiments are carried out on the constructed experimental platform of the elbow joint variable stiffness compliant mechanism. The input shaft is connected to the MG6012E-i8v2 DC brushless servo motor with an internal reducer with a reduction ratio of 1:6. The output shaft is connected to a Forsentek miniature torque transducer, the Forsentek FTE-20 N.m, which is used for the measurement of the output torque of the mechanism. The output shaft is connected to a pendulum, which is connected to a non-contact miniature angle sensor GTE to measure the deflection angle of the pendulum. Thus, the variation of torque and deflection angle can be measured experimentally and saved to the host computer, as shown in Fig. 13.

The VSA possesses reconfigurability and can meet different performance requirements by changing the structural configuration. It is possible to achieve a VSA 1:1 type of mechanical construction by changing the winding way of the elastomer and

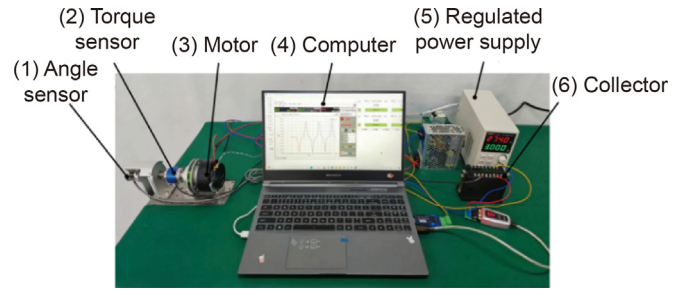


Fig. 13. Torque test of a compliant actuator.

Table 1
Parameters of the proposed virtual deformation model.

Parameter	Value	Parameter	Value	Parameter	Value
T_A	0	x_A	0	k_{AB}	1.7561
T_B	0.72	x_B	0.4100	k_{BC}	6.8864
T_C	3.75	x_C	0.8500	k_{DE}	9.1929
T_D	5.02	x_D	1.0000	k_{EF}	5.5781
T_E	1.93	x_E	0.6639	k_{FG}	1.0887
T_F	0.43	x_F	0.395	k_{GH}	2.2416
T_G	0	x_G	0	k_{HI}	8.2931
T_H	-1.00	x_H	-0.4461	k_{JK}	9.5385
T_I	-4.61	x_I	-0.8814	k_{KL}	6.6620
T_J	-5.66	x_J	-1.0000	k_{LA}	1.6932
T_K	-2.56	x_K	-0.6750	K_+	8.4667
T_L	-0.66	x_L	-0.3898	K_-	8.8533

Table 2
Parameters of the transition phase.

Point	x	τ
P_1	0.8500	3.75
P_2	0.9100	4.60
P_3	0.9300	4.81
P_4	0.9500	4.93
P_5	1.0000	5.02
Q_1	-0.8814	-4.61
Q_2	-0.9153	-5.28
Q_3	-0.9322	-5.47
Q_4	-0.9661	5.62
Q_5	-1.0000	-5.66

the pulleys in a manner that sets the number of pulleys in the input flange to one and the number of pulleys in the output flange to one for a single compliant branch. Thus, six configurations are derived, one of which is selected with $N = 6$, i.e., the compliant unit branch is 6. The resulting movement at a preload force of 5N is used to obtain its deflection angle and output torque, from which the model parameters can be calculated as shown in Table 1 below.

The Maxwell-slip model is used to simulate the non-linearity in the transition phase. The deformation of the model for a point number of 4 is shown in Table 2. The stiffness of each unit as well as the unit limit force are shown in Table 3. The VSA rotates, the angle sensor measures the deflection angle, and the torque sensor measures the output torque (which constitutes the parameters of the model, which are obtained manually). The modified Maxwell-slip model is built up out of m elementary models in parallel. Each element is characterized by a linear spring with a stiffness unit k_i , a maximum force η_i , and a state variable ζ_i . The error between the measured torque and the estimated torque obtained through the proposed hysteresis model is less than 0.3 N.m. It shows that the constructed model is able to accurately estimate the output torque.

Therefore, the code is prepared for the simulation experiments in combination with the previously described formulas and parameter values. The proposed hysteresis model is shown in Fig. 14

Table 3
Parameters of the modified Maxwell-slip model.

Parameter	Value	Parameter	Value
k_1	14.1667	k'_1	8.52
k_2	10.5	k'_2	6.82
k_3	6	k'_3	3.24
k_4	1.8	k'_4	1.18
η_1	0.22	η'_1	0.29
η_2	0.09	η'_2	0.35
η_3	0.116	η'_3	0.27
η_4	0.638	η'_4	0.14

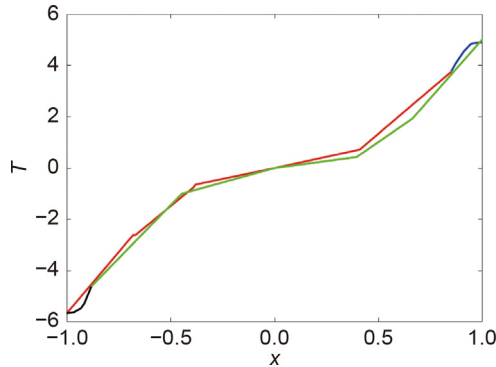


Fig. 14. Proposed hysteresis model.

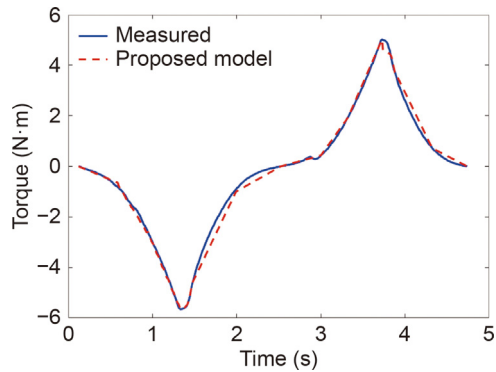


Fig. 15. Torque versus time graph.

below, with a red curve for the ascending phase, a green curve for the descending phase, a blue curve for the transitional phase 1, and a black curve for the transitional phase 2.

A comparison of the torque variation curves between the measured and simulated torque of the proposed model in a certain time period shows the accuracy of the proposed model and the accuracy of the estimated output torque, which verifies the feasibility and validity of the model. Fig. 15 shows the period variation curves of the proposed hysteresis model torque and the measured torque obtained. Fig. 16 shows the variation curves of the torque errors for the two models with a maximum deviation of 0.2 N.m.

The simulation results are compared with the experimental results, as shown in Fig. 17. The average value of torque of the simulated model is 1.7 N.m, and the torque of the model obtained from experimental measurements is 1.8 N.m with a hysteresis error of about 6%, which is able to meet the requirements. The 6% error allows researchers to determine the shape and specifications of the motor. In addition, controlling motor load and temperature, training and optimizing model parameters,

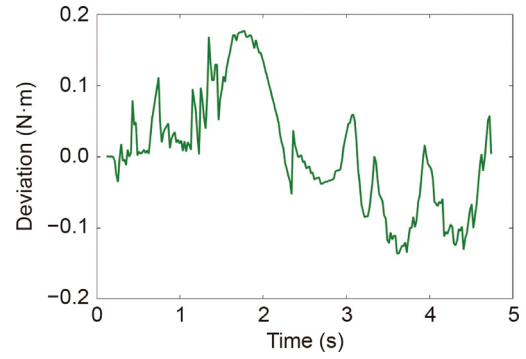


Fig. 16. Torque deviation curve.

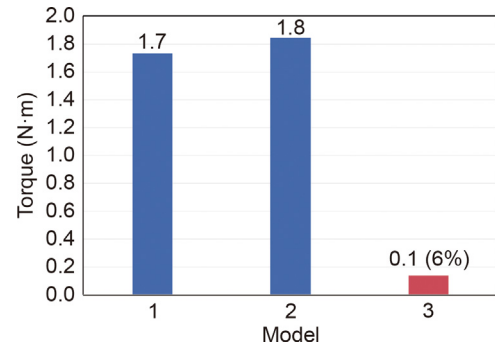


Fig. 17. Comparison of experimentally measured torque and simulated torque: Model 1 is the measured torque, Model 2 is the simulated torque, and Model 3 is the error.

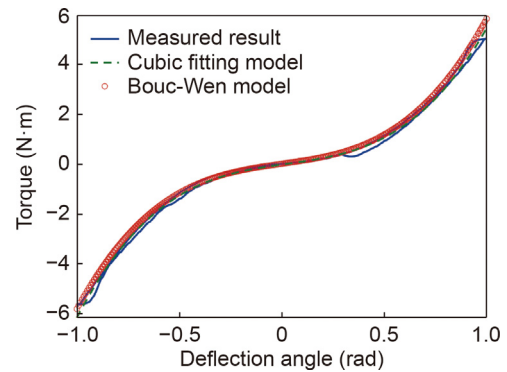


Fig. 18. Comparison of three models.

and using control strategies continue to improve the accuracy of drive motion to eliminate hysteresis.

4.2. Comparison of the proposed model with the cubic fitting model and the Bouc-Wen model

The torque variation in different models is tested to verify the tracking performance of the model. The cubic fitting model and Bouc-Wen model are chosen to compare with the proposed hysteresis model to observe the torque variation of the three models, as shown in Fig. 18. The tracking ability of the three models is also compared, and the tracking error is calculated.

As illustrated in Fig. 19, the maximum deviation of the proposed hysteresis model is 0.2 N.m. The maximum deviation of the cubic fitted model is 0.5 N.m. The maximum deviation of the Bouc-Wen model is greater than 0.5 N.m. Therefore, it has been verified that the proposed model is more accurate. In the

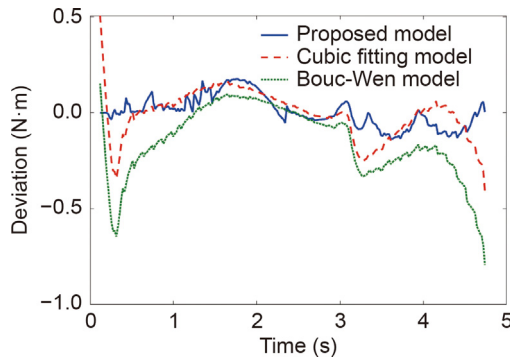


Fig. 19. Torque tracking deviation.

Table 4
Comparison error of torque of two models.

Hysteresis model	MAE (N·m)	MRE (N·m)	RMSE (N·m)
Proposed hysteresis model	0.063	0.187	0.081
Cubic fitted model	0.095	0.271	0.162
Bouc-Wen model	0.182	0.242	0.211

open-loop control mode, the hysteresis model can be calculated offline based on the experimentally obtained data. The law of closed-loop control can be obtained through the compensation calculation of the inverse model after obtaining the hysteresis model, which is a simple and effective method with low cost and higher safety.

A modified Maxwell-slip model combined with virtual deformation is able to simulate the nonlinearities in the hysteresis phenomenon as well as being applicable to other compliant actuators with nonlinearities. At the same time, evaluation metrics such as the Root Mean Squared Error (RMSE) between the measured torque values and the torque values of the proposed model are calculated and compared with other models to verify that the proposed model is able to accurately estimate the output torque.

The parametric indicators of the proposed hysteresis model, cubic fitting model, and Bouc-Wen model were evaluated to measure the prediction accuracy of the three different models. Mean Absolute Error (MAE) estimates the mean absolute error between the predicted and actual values. The MAE is able to directly predict the magnitude of the error for the same order of magnitude. The proposed hysteresis model has a smaller MAE and higher overall prediction accuracy. Meanwhile, Mean Relative Error (MRE) estimates the average relative error between predicted and actual values. The error of the proposed model is closer to 0 with higher accuracy. RMSE is a statistical measure of the overall accuracy of prediction models. A comparison of MRSE calculations to measure prediction accuracy is shown in Table 4. The proposed hysteresis model has smaller RMSE values and higher model accuracy compared to the other models.

5. Examination of the inverse hysteresis model

In order to improve the performance of torque tracking in the actuator, it is necessary to construct the inverse model and set the compensator to reduce hysteresis. Firstly, the hysteresis inverse model is constructed, as shown in Fig. 20. In the inverse hysteresis model, the reference torque is set as input and the virtual deformation value as output. The difference between the inverse hysteresis model and the original hysteresis model is the exchange of horizontal and vertical coordinates, i.e., the transformation of input and output. Therefore, in the case of an inverse hysteresis model, its parameters can be obtained directly from

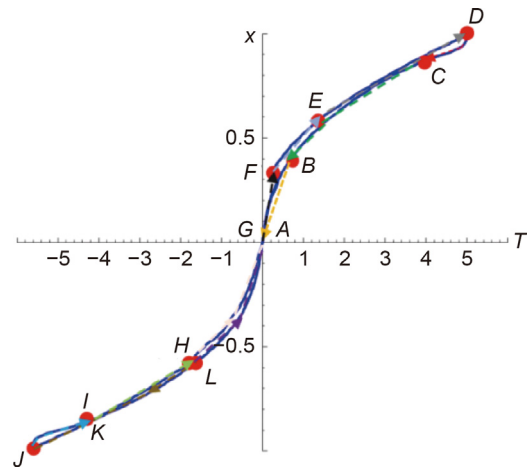


Fig. 20. Description of hysteresis inverse model behavior.

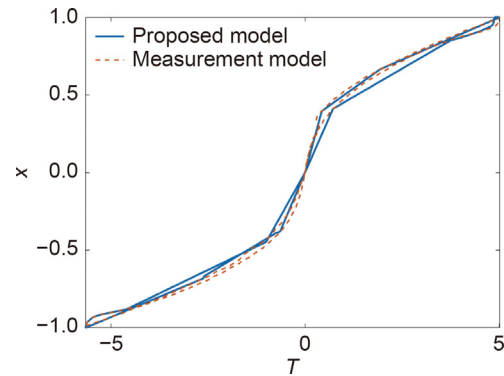


Fig. 21. Comparison between the proposed inverse model and the measurements obtained.

the parameters of the original hysteresis model. At the same time, since the construction method of the inverse hysteresis model still follows the method of the original hysteresis model, the modeling process is simpler and more convenient, which is conducive to improving the compensation performance. By constructing the inverse hysteresis model, the value of the virtual deformation x can be obtained. Thereby, the solution of the inverse kinematics is obtained from the equations of torque and virtual deformation, which lead to the reference trajectory of the motor.

In order to verify the performance of the inverse hysteresis model, the inverse model curves are plotted. Comparing the simulated inverse hysteresis model with the measured inverse model, it is concluded that the two models have the same shape, the same trend of change. The two models basically overlap, as shown in Fig. 21. The deflection angles of the two inverse models are calculated to obtain their variation curves with time as well as the error variation curves, as shown in Figs. 22 and 23. It is learned that the maximum error of the deflection angle is less than 0.15 rad within the period change.

Calculating the RMSE, MRE, and MAE of the above proposed inverse hysteresis model, the inverse cubic fitting model, and the Bouc-Wen model, the proposed inverse hysteresis model has a higher prediction accuracy with a 7% reduction in RMSE, a 16% reduction in MRE, and a 21% reduction in MAE, as shown in Table 5.

6. Conclusions

In this paper, a hysteresis model is presented that utilizes the Maxwell-slip principle and incorporates virtual deformation.

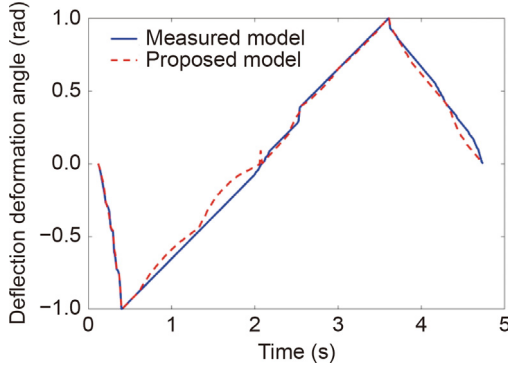


Fig. 22. Comparison of the inverse model deflection angle.

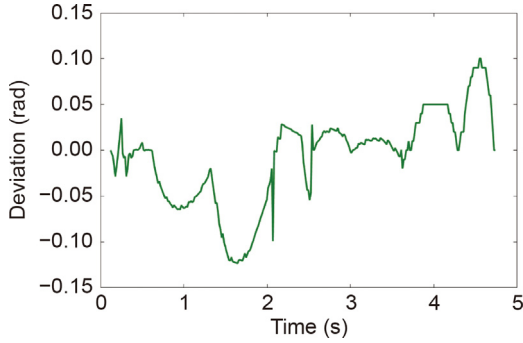


Fig. 23. Deflection angle error.

Table 5
Comparison error of torque of two models.

Hysteresis model	RMSE (rad)	MRE (rad)	MAE (rad)
Proposed inverse hysteresis model	0.051	0.183	0.038
Inverse cubic fitted model	0.056	0.219	0.048
Bouc-Wen model	0.243	0.622	0.217

The model is simple to model, highly accurate, computationally efficient, and easy to construct inverse models. The contributions include:

- (1) The hysteresis phenomenon of VSA is simulated using the Maxwell-slip model in combination with virtual deformation.
- (2) The proposed hysteresis model is compared with the cubic fitting model and the Bouc-Wen model, and it is verified that the model can estimate the driving torque better.
- (3) The inverse model is constructed on the basis of the hysteresis model to calculate the deformation of the deflection angle with time, which lays the foundation for hysteresis compensation.

Although the proposed model is able to model hysteresis well under open-loop control, the effect of the model in closed-loop control systems needs to be considered in future research and applied to exoskeleton robot joints.

CRedit authorship contribution statement

Huibin Qin: Writing – review & editing. **Zefeng Zhang:** Writing – original draft. **Zhili Hou:** Writing – review & editing, Supervision. **Lina Li:** Writing – review & editing, Resources. **Kai Liu:** Investigation. **Shaoping Bai:** Writing – review & editing.

Declaration of competing interest

The authors declare that they have no known competing financial interests or personal relationships that could have appeared to influence the work reported in this paper.

Acknowledgments

This work was supported in part by the Research Project of the Shanxi Scholarship Council of China (2023-135), the 19th graduate science and technology project of the North University of China (20231913), and the Applied Fundamental Youth Science and Technology Research Fund in Shanxi Province of China (202103021223090).

Appendix

The variable stiffness structure of VSA is shown in Fig. 2, and the individual compliant branches are shown in Fig. 3(b). l_1 , l_2 , and l_3 satisfy the following cosine theorem

$$l_2^2 = l_1^2 + l_3^2 - 2l_1l_3 \cos \theta \quad (\text{A.1})$$

The elongation of the elastomer when the elastomer is rotated by θ is $\delta l_e = 2(l_1 + l_2 - l_3)$, where F_e is the elastic tension and T_e is the external equilibrium torque applied to the compliant actuator, which is then obtained as

$$T_e = F_e J_e = F_e \left| \hat{l}_2 \times \vec{l}_1 \right| \quad (\text{A.2})$$

where \hat{l}_2 is the unit vector of \vec{l}_2 , \vec{l}_1 is the parallel vector of l_1 , and J is the displacement generated under the elastic force as

$$J_e = \left| \hat{l}_2 \times \vec{l}_1 \right| = \frac{\partial l_2}{\partial \theta} = \frac{l_1 l_3 \sin \theta}{\sqrt{l_1^2 + l_3^2 - 2l_1 l_3 \cos \theta}} \quad (\text{A.3})$$

Thus, combined with the above equation, the torque can be expressed as

$$T_e = F_e J_e = k[2(l_1 + l_2 - l_3) + x_0] \frac{l_1 l_3 \sin \theta}{l_2} \quad (\text{A.4})$$

In accordance with the principle of virtual work, the equivalent rotational stiffness K_e of the output linkage can be regarded as a linear relationship between the infinitesimal torque δT and the infinitesimal deflection $\delta \theta$. This relationship can be expressed as

$$\delta T = K_e \cdot \delta \theta \quad (\text{A.5})$$

Combining the above equations, the equivalent stiffness of the variable stiffness compliant drive mechanism can be found as

$$K_e = \frac{\delta T}{\delta \theta} = \left(J_e^2 + \frac{J_e}{\theta} \delta l_e \right) k + \frac{J_e}{\theta} F_0 = \underbrace{c_1 k}_{k_1} + \underbrace{c_2 F_0}_{k_2} \quad (\text{A.6})$$

where c_1 and c_2 are

$$\begin{cases} c_1 = \frac{l_1^2 l_3^2 \sin^2 \theta}{l_2} + 2c_2 (l_1 + l_2 - l_3) \\ c_2 = \frac{l_1 l_3 \cos \theta}{l_2} - \frac{l_1^2 l_3^2 \sin^2 \theta}{l_2^3} \end{cases} \quad (\text{A.7})$$

From the stiffness model of the compliant drive mechanism, it can be seen that the stiffness variation of the mechanism is influenced by the physical characteristics of the elastomer, the coupling angle between the input flange and the output flange, and the mechanical structure. The angle θ , the preload force F_0 of the elastic element, and the rod length l are the variables that influence the stiffness model. As can be seen from Eq. (6), the

influence of the stiffness model is divided into two parts. One part is the effect of the elastic element's own stiffness k , which affects the overall stiffness K by changing k_1 ; the other part comes from the elastic element's own preload F_0 , which changes k_2 , thus causing changes in the overall stiffness K . In Eq. (7), c_1 and c_2 are related solely to the geometry of the mechanism and vary nonlinearly with respect to the joint angle θ .

Combining the above equations, the overall stiffness of the variable stiffness compliant drive mechanism with N compliant unit branches and the overall torque model can be solved as in Eq. (8) and Eq. (9)

$$K = Nk \left(J_e^2 + \frac{J_e}{\theta} \delta l_e \right) + N \frac{J_e}{\theta} F_{oe} \quad (\text{A.8})$$

$$T = N (k J_e \delta l_e + J_e F_{oe}) \quad (\text{A.9})$$

According to Hooke's law, F_e can be expressed as

$$F_e = k \delta l_e + F_0 \quad (\text{A.10})$$

where k is the stiffness of the elastomer and F_0 is the initial preload force of the elastomer, which can be expressed as

$$F_0 = k x_0 \quad (\text{A.11})$$

Therefore, we can get

$$T = k [12 (l_1 + l_2 - l_3) + x_0] \frac{l_1 l_3 \sin \theta}{l_2} \quad (\text{A.12})$$

References

- [1] Z.Y. Yang, S. Guo, A hybrid motion stiffness control of variable stiffness actuator for upper limb elbow joints rehabilitation, in: 19th IEEE International Conference on Mechatronics and Automation, ICMA, IEEE, 2022, pp. 1324–1328.
- [2] Q. Fu, Y. Wang, B. Duan, Modeling and control of upper limb rehabilitation system based on variable stiffness joints, in: 20th IEEE International Conference on Mechatronics and Automation, ICMA, IEEE, 2023, pp. 409–413.
- [3] Z. Du, Y. Xiao, W. Dong, Modeling method for robotic arm joints with friction gap hysteresis, *Robot* 33 (5) (2011) 539–545.
- [4] A.B. Farid, L. Vincent, S. Jan, The generalized Maxwell-slip model: A novel model for friction simulation and compensation, *IEEE Trans. Autom. Control* 50 (2005) 1883–1887.
- [5] D.D. Rizos, S.D. Fassois, Maxwell slip model based identification and control of systems with friction, in: 44th IEEE Conference on Decision and Control, and the European Control Conference, IEEE, pp. 4578–4583.
- [6] M. Ruderman, F. Hoffmann, T. Beatram, Modeling and identification of elastic robot joints with hysteresis and backlash, *IEEE Trans. Ind. Electron.* 56 (2009) 3840–3847.
- [7] Z.Y. Nie, R.J. Liu, Q.G. Wang, D.S. Guo, Y.J. Ma, Y.H. Lan, Novel identification approach for nonlinear systems with hysteresis, *Nonlinear Dynam.* 95 (2) (2019) 1053–1066.
- [8] A. Laudani, F. R. Fulginei, A. Salvini, Bou–Wen hysteresis model identification by the metric-topological evolutionary optimization, *IEEE Trans. Magn.* 50 (2) (2014) 621–624.
- [9] G. Wang, G. Chen, F. Bai, Modeling and identification of asymmetric Bou–Wen hysteresis for piezoelectric actuator via a novel differential evolution algorithm, *Sens Actuators A* 235 (2015) 105–118.
- [10] R. Dhauadi, F.H. Ghorbel, P.S. Gandhi, A new dynamic model of hysteresis in harmonic drives, *IEEE Trans. Ind. Electron.* 50 (6) (2003) 1165–1171.
- [11] W. Choi, J. Won, J. Lee, J. Park, Low stiffness design and hysteresis compensation torque control of SEA for active exercise rehabilitation robots, *Nonlinear Dynam.* 95 (2018) 1053–1066.
- [12] I.D. Mayergoyz, *Mathematical Models of Hysteresis and their Applications*, New York, 2003.
- [13] V. Hassani, T. Tjahjowidodo, T.N. Do, A survey on hysteresis modeling, identification and control, *Mech. Syst. Signal Process.* 49 (1–2) (2014) 209–233.
- [14] S. Zschack, S. Buchner, A. Amthor, C. Ament, Maxwell slip based adaptive friction compensation in high precision applications, in: 38th Annual Conference on IEEE Industrial Electronics Society, IECON, 2012, pp. 2331–2336.
- [15] W. Chen, L. Zhou, J. Wang, Z. Zhao, W. Chen, S. Bai, A Maxwell-slip based hysteresis model for nonlinear stiffness compliant actuators, *IEEE Trans. Ind. Electron.* 69 (11) (2022) 11510–11520.
- [16] Z. Li, S. Bai, A novel revolute joint of variable stiffness with reconfigurability, *Mech. Mach. Theory* 133 (2019) 720–736.
- [17] Z. Li, S. Bai, O. Madsen, W. Chen, J. Zhang, Design, modeling and testing of a compact variable stiffness mechanism for exoskeletons, *Mech. Mach. Theory* 151 (2020) 103905.
- [18] R. Liu, Z. Zheng, H. Qin, Z. Li, S. Bai, Design and performance analysis of variable stiffness compliant driving mechanism, *J. Mech. Transm.* 46 (12) (2022) 53–59.
- [19] W. Duan, H. Qin, R. Liu, Z. Li, S. Bai, Design and performance analysis of reconfigurable variable stiffness compliant actuators, *Chin. J. Eng. Des.* 30 (2) (2023) 1–9.
- [20] H.S. Jan, *Smart Technologies for Safety Engineering*, Hoboken, NJ, USA, 2008, pp. 11–35.